

## THE SN 1006 REMNANT: OPTICAL PROPER MOTIONS, DEEP IMAGING, DISTANCE, AND BRIGHTNESS AT MAXIMUM

P. FRANK WINKLER<sup>1</sup>, GAURAV GUPTA<sup>2</sup>Department of Physics, Middlebury College, Middlebury, VT 05753  
winkler@middlebury.edu

AND

KNOX S. LONG<sup>1</sup>

Space Telescope Science Institute, Baltimore MD 21218

*Submitted: 30 July 2002*

## ABSTRACT

We report the first measurement of proper motions in the SN 1006 remnant (G327.6+14.6) based entirely on digital images. CCD images from three epochs spanning a period of 11 years are used: 1987 from Las Campanas, and 1991 and 1998 from CTIO. The filaments in SN 1006 are non-radiative, appearing only in the Balmer lines of hydrogen. Delicate filaments—probably thin sheets seen in projection—delineate the shock front along the northwest rim of the remnant. We use the center of curvature of the filaments to define a convenient geometry, and integrate along short segments to obtain one-dimensional profiles. These remain unchanged, within seeing and statistical errors, from one epoch to another. Measuring the shift in a direction perpendicular to the filaments, we obtain proper motions of  $280 \pm 8$  mas yr<sup>-1</sup> along the entire length where the filaments are well defined, with little systematic variation along the filaments. In addition to the measurements of the well-defined filaments in the NW of SN 1006, we also report very deep H $\alpha$  imaging observations of the entire remnant that clearly show very faint emission surrounding almost the entire shell, as well as some diffuse emission regions in the (projected) interior.

Combining the proper motion measurement with a recent measurement of the shock velocity based on spectra of the same filaments by Ghavamian *et al.* leads to a distance of  $2.17 \pm 0.08$  kpc to SN 1006. Several lines of argument suggest that SN 1006 was a Type Ia event, so the improved distance measurement can be combined with the peak luminosity for SNe Ia, as recently determined for events in galaxies with Cepheid-based distances, to calculate the apparent brightness of the spectacular event that drew wide attention in the eleventh century. The result,  $V_{max} = -7.5 \pm 0.4$ , lies squarely in the middle of the wide range of estimates based on the historical observations.

*Subject headings:* ISM: individual (SN 1006, SNR G327.6+14.6) — shock waves — supernovae:  
individual (SN 1006) — supernova remnants

## 1. INTRODUCTION

Early in the eleventh century, the supernova of 1006 C.E. attracted wide attention, and it is probably the brightest stellar event in recorded human history (Stephenson *et al.* 1977). Almost a millennium later, the supernova remnant (SNR) that this event produced has gradually emerged as an object of great astrophysical interest. The remnant of SN 1006, G327.6+14.6, was first identified through its radio emission by Gardner & Milne (1965). X-ray emission was detected by Winkler & Laird (1976), and very soon afterward van den Bergh (1976) reported faint optical filaments associated with SN 1006. More recent radio maps (Reynolds & Gilmore 1986; Moffett *et al.* 1993) show a somewhat barrel-shaped shell, 30' in diameter and brightest along the NE and SW limbs. X-ray images (Willingale *et al.* 1996; Winkler & Long 1997, hereafter WL97) show a similar structure to that seen in the radio, while optical emission is limited almost entirely to delicate filaments extending some 15' along the NW rim of the remnant shell—a region that is generally faint

in both X-rays and radio. The optical spectrum shows only Balmer lines of hydrogen (Schweizer & Lasker 1978), indicative of a nonradiative shock propagating into partially neutral interstellar material (*e.g.* McKee & Hollenbach 1980).

Renewed interest in the SN 1006 remnant was stimulated with the discovery by Koyama *et al.* (1995), based on *ASCA* data, that the strongest X-ray emission, from the NE and SW limbs, has a hard, featureless, non-thermal spectrum characteristic of synchrotron radiation, while the X-rays from the interior and from the NW and SE limbs are much softer and are thermal in character. These data strongly suggested that in the NE and SW, electrons are accelerated to TeV energies by the first-order Fermi mechanism in the supernova shock. Furthermore, since the same mechanism will accelerate nuclei as well, the Koyama *et al.* (1995) data provided the first solid observational evidence that supernova shocks produce cosmic rays. The supernova-cosmic ray connection was solidified with the demonstration of detailed correspondence between X-ray and radio morphology along the NE and SW limbs of

<sup>1</sup> Visiting Astronomer, Cerro Tololo Inter-American Observatory. CTIO is operated by AURA, Inc. under contract to the National Science Foundation.

<sup>2</sup> Present Address: Department of Mechanical and Aerospace Engineering, Cornell University, Ithaca, NY 14853

TABLE 1  
IMAGING OBSERVATIONS OF SN 1006.

| Date        | Telescope  | CCD             | Scale<br>('' pixel <sup>-1</sup> ) | Filter          |                     | Exposure<br>(s) | Seeing<br>(FWHM) | Observers                 |
|-------------|------------|-----------------|------------------------------------|-----------------|---------------------|-----------------|------------------|---------------------------|
|             |            |                 |                                    | $\lambda_0$ (Å) | $\Delta\lambda$ (Å) |                 |                  |                           |
| 1987 Apr 26 | LCO 2.5-m  | TI 800 × 800    | 0.41                               | 6572            | 52                  | 3 × 1000        | 1''0             | Long & Blair <sup>a</sup> |
| 1991 Apr 19 | CTIO 4-m   | Tek 1024 × 1024 | 0.47                               | 6563            | 30                  | 600             | 1''1             | Winkler & Long            |
| 1998 Jun 23 | CTIO 0.9-m | Tek 2048 × 2048 | 0.40                               | 6566            | 24                  | 9 × 1000        | 1''1             | Winkler & Long            |

<sup>a</sup>William P. Blair, Johns Hopkins University.

SN 1006 (WL97) and especially by the discovery of  $\gamma$ -ray emission from the NE limb of SN 1006 by Tanimori et al. (1998).

The optical filaments of SN 1006 provide a rich opportunity to investigate the nature of the nonradiative shock and the environment into which it propagates. The Balmer line profile consists of two components: a broad component that results from neutral atoms that penetrate the shock and then undergo charge exchange with hot, post-shock protons to produce a population of hot neutrals, and a narrow component from simple collisional excitation of the ambient neutral atoms (Chevalier & Raymond 1978; Chevalier et al. 1980). Ghavamian et al. (2002) present detailed spectra and models that lead to a precise measurement of the shock velocity in the NW region of SN 1006:  $v_s = 2890 \pm 100$  km s<sup>-1</sup>.

The present paper presents a measurement of the proper motion of the NW filaments of SN 1006 with a precision of  $\sim 2\%$ , comparable to that of the recent shock velocity measurement. The geometry of the NW filaments—apparently thin sheets seen almost exactly edge-on—is ideally suited to measuring the remnant’s expansion. Proper motion of the optical filaments in SN 1006 was first reported only five years after their discovery (Hesser & van den Bergh 1981), but a reasonably precise measurement had to wait for a longer baseline. Long et al. (1988, hereafter LBV88) combined first-epoch photographic plates and CCD images taken 11 years later to obtain a measurement of  $0.30 \pm 0.04$  arcsec yr<sup>-1</sup>. We use the same 1987-epoch CCD image used by LBV88, together with subsequent CCD images from epochs 1991 and 1998, to obtain a much more precise measurement—the first relying entirely on digital images. Section 2 of the paper describes the observations themselves. Section 3 discusses two different algorithms we have employed to measure the filamentary motion and presents the results. Section 4 presents new, deep observations of very faint H $\alpha$  emission that outlines the entire shell of the SN 1006 remnant, as first reported by WL97. In the final three sections we discuss some implications of the present measurements, including a comparison with proper motion measurements carried out in other regimes of the electromagnetic spectrum. The combination of our new proper-motion measurements and the shock-velocity determined by Ghavamian et al. (2002) leads directly to a distance of  $2.17 \pm 0.08$  kpc to SN 1006. This distance, together with recent determinations of the peak absolute magnitudes for Type Ia supernovae, provides an estimate of the apparent brightness of SN 1006 at maximum that is significantly more precise than earlier ones.

<sup>3</sup> IRAF is distributed by the National Optical Astronomy Observatories, which is operated by the AURA, Inc. under cooperative agreement with the National Science Foundation.

## 2. OBSERVATIONS

Narrow-band imaging observations of SN 1006 in H $\alpha$  were carried out at three epochs, 1987, 1991, and 1998, using CCDs on telescopes at Las Campanas and CTIO. The observational details are summarized in Table 1. All three sets of observations were carried out under good seeing conditions; individual stars show profiles with FWHM near 1''. The first-epoch image for the current study is identical with the one used for the second epoch by LBV88 and appearing in Figures 1 and 3a of that paper, and the 1991-epoch image from the Blanco 4-m telescope appears as part of the mosaic shown as Figure 2 in WL97. The data were reduced using standard IRAF<sup>3</sup> procedures of bias subtraction and flat fielding.

## 3. PROPER MOTION MEASUREMENT

The initial step in measuring filamentary proper motions is to align images from different epochs so they are as perfectly registered as possible, using the stars as fiducial markers. Then the filamentary motions are apparent as position shifts from one epoch to another. In their measurement, LBV88 simply used cursor readings at several points along the filament to compare the positions at two epochs. Since their first-epoch image came from a digitized photographic plate, they found that this technique was as accurate as any other; nevertheless, this limited the precision of their measurement to  $\sim 1$  pixel = 0''.4 or  $\pm 0.037$  arcsec yr<sup>-1</sup> over their 11-year baseline.

With multiple epochs of CCD data, we can take a more sophisticated approach to obtain measurements with a precision of a small fraction of a pixel. The basic idea is first to obtain a one-dimensional profile in a direction perpendicular to a short segment of filament at multiple epochs. Then we shift the profile from one epoch relative to that at another and measure how well they match as a function of the shift. The shift that gives the best match indicates the proper motion between the two epochs for that segment. This section describes the steps in some detail.

### 3.1. Image Registration

We first aligned the images from all three epochs on a common coordinate system using tasks in the IRAF “imcoords” and “immatch” packages. In order to achieve optimum resolution, we transformed all the images to a standard coordinate system at a scale of exactly 0''.10 pixel<sup>-1</sup>, subsampling the original images by about a factor of 4. We

chose the 1998 epoch as the reference image, since it has a 13.7 field of view, widest of the three epochs in the set, and minimal distortion across the field. We obtained plate solutions for each of the nine individual 1998 frames, all of which were taken on somewhat different centers, using stars from the UCAC1 catalog (Zacharias et al. 2000). The simplest 4-parameter solution ( $x$ - and  $y$ -translation, rotation, and pixel scale) gave excellent fits. We then transformed the individual frames to our adopted standard coordinate system, using simple linear interpolation for the subsampling, and combined them into a single reference image.

We then transformed the images from the 1987 and 1991 epochs to match the reference image. Here the transformation was less straightforward, due to the lack of flatness that characterized the TI chip used in 1987 and the curvature of the Blanco 4m prime-focus camera used in 1991. For fiducial points, we used a set of over 100 stars, located in a band straddling the NW filaments, that are unsaturated in all three images. After allowing quadratic distortion terms, we obtained good fits, with RMS residuals of 0".06 and 0".04 for the 1987 and 1991 epoch images, respectively. (An exception is the extreme western edge of the 1987 image, which shows larger distortions where the TI chip curvature was the worst and the stars were poorly focused. This region was not used in our analysis.)

We note that the rebinned images have somewhat lower (by a factor of about 1.4) sky noise than the original ones, for which the sky noise was completely consistent with Poisson statistics. This results because of correlations introduced in the image transformation process (Fruchter & Hook 2002) and averaging of flux across multiple pixels. In our subsequent analysis, in which we use uncertainties in the pixel values as the basis for calculating  $\chi^2$  values, we have adjusted these uncertainties from their purely Poisson-statistical values to reflect the averaging effect and to be consistent with the actual distribution in the rebinned, registered images.

Once the images from the three epochs have been registered, the proper motion of the NW filaments is apparent. This is illustrated dramatically in Figure 1: the left panel shows a section of the 1998 image, while the right panel shows the difference between the 1998 and 1987 images.

### 3.2. One-dimensional Profiles

We sought to measure one-dimensional profiles across the narrow width of the filaments, *i.e.*, along their direction of motion. In order to get profiles with both high angular resolution across the filaments and reasonable signal-to-noise, we must integrate for some distance along them. Fortunately, the geometry of the NW filaments is very favorable; their crisp, well-defined portion lies very nearly along the arc of a circle, centered at  $\alpha(2000) = 15^{\text{h}}03^{\text{m}}16^{\text{s}}.2$ ,  $\delta(2000) = -42^{\circ}00'30''$  (WL97). (This is *not* the center of the SNR shell, but rather the center of curvature for the brightest optical filaments.) From this center we defined 11 sectors, each  $2^{\circ}$  in azimuth, and took a radial profile for the portion of the filament within each sector. Each bin of a profile represents a very thin slice of width 0".10 integrated along  $2^{\circ}$  in azimuth, an arc length of about 40 arcsec. The geometry is illustrated in Fig. 2.

Before measuring the radial profiles for the filament, we first had to remove the stars from the region of interest; otherwise, they would contaminate the profiles and confuse the measurement. After the images had been aligned, stars within the profile region were subtracted using DAOPHOT techniques, followed by manual editing. Then the radial profiles were calculated using the IRAF/PROS task "imcntr" to measure the average counts per pixel along each of 350 0".1-wide slices. Profiles were obtained for all eleven sectors at the 1991 and 1998 epochs. With the 1987-epoch image, however, the smaller field of view and distortions near the western edge limited us to using profiles for only eight of the sectors. A common scaling factor was applied to all the profiles from each epoch to account for differences in exposure time and sensitivity among the observations from different instruments at the three epochs. For each profile we also calculated the uncertainty in each of the bins based on Poisson statistics from the original images (using the known gain and read-out noise), adjusted downward slightly to reflect the averaging that accompanied rebinning (see previous section). As an important check on this procedure, we found that the actual measured rms dispersion for the sky portion of the profiles (*i.e.*, in regions inside or outside the filaments, where the counts per pixel appeared to be constant, on average) agreed well with the uncertainty values we had calculated. Scaled profiles for one sector for epochs 1987 and 1998 are shown in Fig. 3.

### 3.3. Measuring Shifts between Epochs

Once scaled profiles like the ones shown in Fig. 3 have been calculated, it remains merely to shift the profile from one epoch outward in the radial direction to achieve the best match with the profile at a later epoch. Since the profiles are well-defined and have high signal-to-noise, simply sliding profiles from different epochs back and forth and matching them by eye is sufficient to measure the shift to within a few tenths of an arcsec; however, digital techniques make more precise measurement possible. We have applied two different techniques, outlined below, which give virtually identical results.

#### 3.3.1. Method I: Correlation Analysis

The problem of shifting a one-dimensional image by a variable offset to achieve the best match to a template image occurs often in spectroscopy; *e.g.*, in calculating the redshifts of distant galaxies. Tonry & Davis (1979) have presented a procedure based on correlation analysis for calculating the optimum redshift of a spectrum. We followed a virtually identical procedure to obtain the pixel shift of both the 1987 and 1991 profiles relative to the corresponding profiles in the 1998 reference image. This method is quite straightforward to implement using the IRAF task "fxcor" to obtain a correlation in terms of profile bins, but in our case it does not lead to reliable estimates for the uncertainty in the measured value for pixel shift between epochs.

#### 3.3.2. Method II: Minimum $\chi^2$ Analysis

We have also used an independent approach based on calculating directly the  $\chi^2$  probability that two observed profiles from different epochs represent the same underlying physical profile, shifted by an amount treated as a

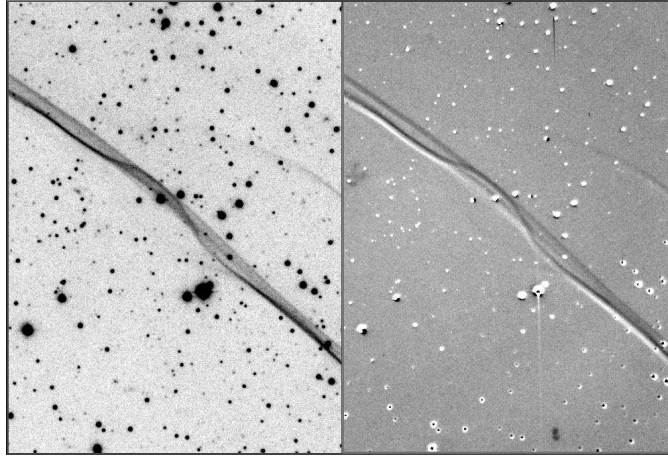


FIG. 1.— (Left) A portion of the NW rim of the SN 1006 remnant in  $H\alpha$  showing the prominent filaments at epoch 1998. (Right) The same image with one from epoch 1987 subtracted, so that at the earlier epoch the filaments appear white, and at the later one, black.

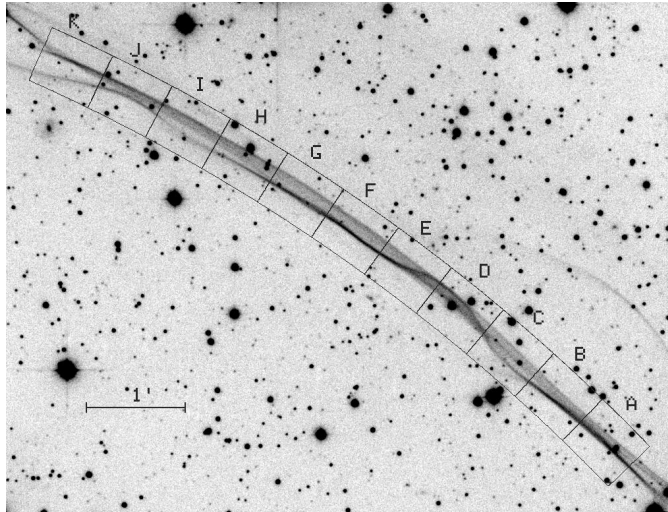


FIG. 2.— The 1998-epoch  $H\alpha$  image of the NW filaments in SN 1006, showing the 11 sectors (A–K) for which radial profiles and proper motions were measured. (For the 1987-epoch image, only sectors B–I were usable.)

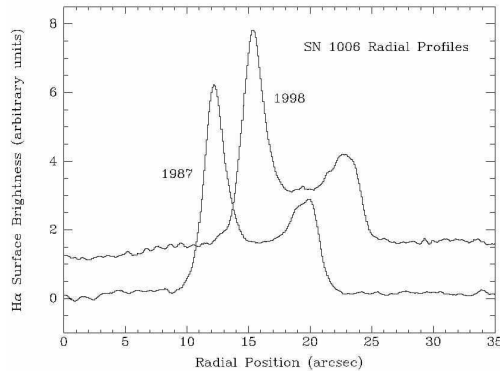


FIG. 3.— Radial profiles of a portion of the NW filament of SN 1006 (sector F of Fig. 2) at epochs 1987 and 1998. (The 1998 profile is shifted upward for clarity.) For this and other sectors the profile shapes are virtually identical at different epochs except for the obvious radial displacement.

parameter in the fit. Let  $x_1(k)$  and  $x_2(k)$  represent the observed profiles in discrete bins ( $k$ ) at epochs 1 and 2, and  $\sigma_1(k)$  and  $\sigma_2(k)$  represent the uncertainties at each bin. These uncertainties are traceable to Poisson statistics and the read noise of the chips, with some adjustment as discussed in Section 3.2. If  $x_1(k)$  and  $x_2(k)$  are simply two independent samples of the same underlying physical distribution, then we expect a  $\chi^2$ -distribution with  $n$  degrees of freedom for

$$\chi^2 = \sum_{k=1}^n \frac{(x_1(k) - x_2(k))^2}{\sigma_1^2(k) + \sigma_2^2(k)}, \quad (1)$$

where  $n$  is the number of bins in the profile (*e.g.*, Bevington & Robinson 1992). For the case in which one profile is offset relative to another, we introduce an offset parameter,  $l$ , in the bin index and calculate  $\chi^2$  as a function of  $l$ ,

$$\chi^2(l) = \sum_{k=1}^n \frac{(x_1(k+l) - x_2(k))^2}{\sigma_1^2(k+l) + \sigma_2^2(k)}. \quad (2)$$

The minimum for  $\chi^2(l)$  occurs for the value of  $l$  at which the two profiles best match. Furthermore, since this represents a fit with  $l$  as a single “interesting” parameter, the  $1\sigma$  uncertainty limits will occur for values of  $l$  that give  $\chi_{min}^2 + 1$  (Lampton et al. 1976; Avni 1976). And finally, the reduced  $\chi^2$  value,  $\chi_\nu^2 = \chi_{min}^2/\nu$ , where  $\nu$  is the number of degrees of freedom, gives a quantitative measure of how well the profiles at different epochs coincide. Here  $\nu = n - 3$ , the number of bins considered, less the number of free parameters. (In addition to the “interesting” parameter  $l$ , the sky level and the amplitude scaling factor also represent parameters that are adjusted; in practice  $n \gg 3$ , so this detail is insignificant.) For large  $\nu$ , one expects  $\chi_\nu^2 \sim 1$  if the expanding filaments remain essentially constant in shape over the span of our observations.

To calculate the displacements, we chose the 1998 image as the reference, and took 200 bins (a  $20''$  distance), roughly centered on the filament peak, from the profile for each sector. We did the comparison of the 1987 and 1991 profiles with the 1998 one for the same sector by, in effect, sliding a moving 200-bin window along the earlier profile and calculating  $\chi^2(l)$  by Eq. 2. For each profile pair we took the five  $\chi^2(l)$  values closest to the minimum and fitted a parabola, in order to obtain a displacement

measurement that is not limited by the granularity of the  $0''.1$  bins.

### 3.4. Results

The results from these measurements are summarized in Table 2. Individual values for the shift in filament position, as measured both by the correlation method and by minimizing  $\chi^2$ , are given for each sector. In every case the two methods give virtually identical results. The values for the proper motion,  $\mu$  (columns 6 and 10), use a simple average of the shifts obtained by the two methods, divided by the baseline between epochs. Measurements are presented for both the 1987–1998 and 1991–1998 combinations; the third pair, 1987–1991, is not independent of the other two and, since it represents the shortest baseline, is omitted.

The uncertainties in measured position shifts, columns 4 and 8 of Table 2, were estimated by using the  $\chi_{min}^2 + 1$  criterion for a single interesting parameter, as discussed in the preceding section. The same values are carried over to give the uncertainties in  $\mu$ , columns 6 and 10. The minimum- $\chi^2$  values per degree of freedom,  $\chi_\nu^2$  (columns 5 and 9), are close to 1, as expected provided that the morphology of the filaments has not changed appreciably over the period of our observations and that we have properly characterized the data. This, in turn, lends confidence that our uncertainty estimates are at least approximately correct.

A second criterion that indicates that our uncertainty estimates are reasonable is comparison between the two measurements of  $\mu$  over independent baselines, 1987–98 and 1991–98. In almost all of the eight sectors where we have measurements over two independent baselines, the two values for  $\mu$  are consistent, within the uncertainties. These results are illustrated graphically in Fig. 4. The values for the mean proper motion,  $\langle \mu \rangle$  (column 11 of Table 2), in each sector are obtained from a weighted (inversely as the variance) mean of the measurements over the two independent baselines.

As one moves along the filaments in azimuth, there is some evidence for a variation in the rate of expansion, as shown in Figure 4. What is most apparent, however, is that any such variation is slight, if present at all. Over the azimuth range  $314^\circ$ – $336^\circ$ , all the measurements lie within the range  $280 \pm 8$  mas yr $^{-1}$ , a variation of  $< 3\%$ . The new measurements all agree with the mean value of

TABLE 2  
PROPER MOTION MEASUREMENTS FOR THE NW BALMER FILAMENTS IN SN 1006.

| Sector<br>(1) | Azimuth<br>(2) | 1987–1998 Measurement <sup>a</sup>           |   |                          |   | 1991–1998 Measurement <sup>b</sup>           |   |                          |  | Mean <sup>c</sup>  |
|---------------|----------------|--|---|--------------------------|---|--|---|--------------------------|--|--|
|               |                | Correlation<br>Shift <sup>d</sup> (″)<br>(3) | $\chi^2$ Shift <sup>e</sup><br>(″)<br>(4) | $(\chi^2)_{\min}$<br>(5) | $\mu^f$<br>(mas yr <sup>-1</sup> )<br>(6) | Correlation<br>Shift <sup>d</sup> (″)<br>(7) | $\chi^2$ Shift <sup>e</sup><br>(″)<br>(8) | $(\chi^2)_{\min}$<br>(9) | $\mu^f$<br>(mas yr <sup>-1</sup> )<br>(10) | $\langle \mu \rangle$<br>(mas yr <sup>-1</sup> )<br>(11) |
| A             | 314°–316°      |  |   |                          |   | 2.068  | 2.070(15)                                 | 1.20                     | 288.2 ± 2.1                                | 288.2 ± 2.1  |
| B             | 316°–318°      | 3.200  | 3.209(19)                                 | 1.89                     | 287.1 ± 1.7                               | 2.036  | 2.038(16)                                 | 1.04                     | 283.7 ± 2.2                                | 285.2 ± 1.4  |
| C             | 318°–320°      | 3.118  | 3.180(32)                                 | 1.50                     | 282.2 ± 2.9                               | 2.044  | 2.081(28)                                 | 1.89                     | 287.3 ± 3.9                                | 284.0 ± 2.3  |
| D             | 320°–322°      | 3.091  | 3.087(21)                                 | 0.66                     | 276.8 ± 1.9                               | 1.935  | 1.934(19)                                 | 1.29                     | 269.4 ± 2.6                                | 274.3 ± 1.5  |
| E             | 322°–324°      | 3.126  | 3.128(18)                                 | 1.78                     | 280.2 ± 1.6                               | 1.991  | 1.992(19)                                 | 0.72                     | 277.4 ± 2.6                                | 279.4 ± 1.4  |
| F             | 324°–326°      | 3.156  | 3.156(13)                                 | 0.62                     | 282.8 ± 1.1                               | 2.040  | 2.042(12)                                 | 0.53                     | 284.2 ± 1.7                                | 283.2 ± 1.0  |
| G             | 326°–328°      | 3.170  | 3.172(16)                                 | 1.03                     | 284.1 ± 1.4                               | 2.029  | 2.034(13)                                 | 0.89                     | 282.9 ± 1.8                                | 283.7 ± 1.1  |
| H             | 328°–330°      | 3.216  | 3.219(18)                                 | 0.83                     | 288.3 ± 1.6                               | 2.038  | 2.042(18)                                 | 0.82                     | 284.1 ± 2.5                                | 287.1 ± 1.4  |
| I             | 330°–332°      | 3.079  | 3.095(22)                                 | 0.83                     | 276.6 ± 2.0                               | 1.982  | 2.001(21)                                 | 0.83                     | 277.4 ± 2.9                                | 276.8 ± 1.6  |
| J             | 332°–334°      |  |   |                          |   | 1.999  | 1.999(17)                                 | 0.71                     | 278.4 ± 2.4                                | 278.4 ± 2.4  |
| K             | 334°–336°      |  |   |                          |   | 1.952  | 1.957(16)                                 | 1.00                     | 272.2 ± 2.2                                | 272.2 ± 2.2  |

<sup>a</sup>11.16-year baseline.

<sup>b</sup>7.18-year baseline.

<sup>c</sup>Weighted mean of the 1987–98 and 1987–98 measurements.

<sup>d</sup>Shift in filament position between epochs measured by the correlation method.

<sup>e</sup>Shift in filament position between epochs measured by minimizing  $\chi^2$ ; uncertainty in the last two digits shown in parentheses.

<sup>f</sup>Mean of measurements by the correlation and minimum- $\chi^2$  methods, divided by the baseline.

TABLE 3  
WIDE-FIELD IMAGING OBSERVATIONS OF SN 1006.

| Date           | Telescope    | CCD             | Scale                    | Filter          |                     | Exposure<br>(s) |
|----------------|--------------|-----------------|--------------------------|-----------------|---------------------|-----------------|
|                |              |                 | (″ pixel <sup>-1</sup> ) | $\lambda_0$ (Å) | $\Delta\lambda$ (Å) |                 |
| 1998 Jun 18-20 | CTIO Schmidt | Tek 2048 × 2048 | 2.32                     | 6567            | 29                  | 16 × 600        |
| 1998 Jun 18-20 | CTIO Schmidt | Tek 2048 × 2048 | 2.32                     | 6852            | 95                  | 16 × 180        |
| 1998 Jun 24    | CTIO Schmidt | Tek 2048 × 2048 | 2.32                     | 6557            | 25                  | 13 × 600        |
| 1998 Jun 24    | CTIO Schmidt | Tek 2048 × 2048 | 2.32                     | 6852            | 95                  | 13 × 180        |

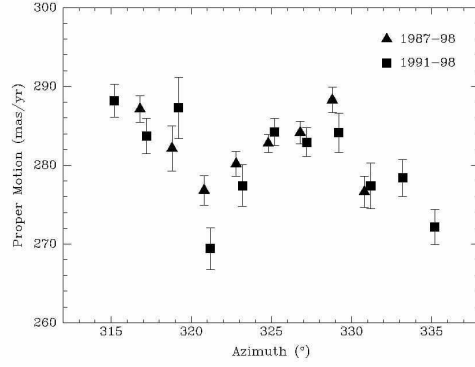


FIG. 4.— Proper motions of the SN 1006 filaments, measured in  $2^\circ$  azimuthal sectors, over baselines 1987–98 (triangles) and 1991–98 (squares). Points for the two baselines at the same azimuth are displaced horizontally for clarity.

$300 \pm 40 \text{ mas yr}^{-1}$  reported by LBV88 for 10 positions along the filaments—with an azimuth range very similar to the one where our measurements were made. Although LBV88 reported proper-motion values ranging from 220 to  $330 \text{ mas yr}^{-1}$ , all but one of their ten measurements were consistent (within  $\pm 1\sigma$ ) with no variation along the filaments. The only other previous measurement is that by Hesser & van den Bergh (1981), who found a mean proper motion of  $390 \pm 60 \text{ mas yr}^{-1}$ , but with large scatter among their 11 individual values: 140 to  $850 \text{ mas yr}^{-1}$ . The Hesser & van den Bergh (1981) measurement was made by scanning plates from two epochs perpendicular to the direction of the filaments with a PDS microdensitometer and comparing the profiles visually. This measurement suffered from the short (5 yr) baseline between epochs and from poor seeing on the second-epoch plate. The LBV88 measurement was made by digitizing the first-epoch image, aligning the images from the two epochs, and then simply measuring the position of the filament on the screen using an image cursor. We are confident that our measurement, based on CCD images from three different epochs, all with excellent seeing, and using two different but consistent digital techniques to measure the shifts, has produced a much more precise result.

#### 4. DEEP IMAGING: FAINT, DIFFUSE $H\alpha$ EMISSION

In addition to the prominent Balmer-dominated filaments in the NW of SN 1006, there is also much fainter, more diffuse, Balmer emission surrounding almost the entire shell and at some places in the interior. Discovered in CCD images obtained from the CTIO 0.6-m Curtis Schmidt telescope, this emission was reported in WL97. In the same 1998 CTIO observing run where we obtained the 0.9-m images for the proper-motion study, we also obtained a long series of images from the Schmidt, in order to reveal the full extent of the faint emission. Images were obtained through two different  $H\alpha$  filters (a backup  $H\alpha$  filter was used for the 18–20 June observations since our primary filter was in use at the 0.9-m) and through a matched red continuum filter, to facilitate subtraction of the stars. The observational details are given in Table 3.

Figure 5 shows the  $H\alpha$  image after continuum subtraction. Continuum subtraction was done separately for the 18–20 June and the 24 June data, and then the subtracted images were combined. The latter image shows, in ad-

dition to the “bright” NW filaments, a more diffuse and much fainter outline of  $H\alpha$  emission extending around almost the entire shell of SN 1006. Also evident are many features, mostly diffuse emission but with a few well-defined filaments, within the shell (as seen in projection). Some of these faint features were evident in Figures 1b and 1c of WL97, but the new images reveal far more detail. Although the present images and those from 1993 shown in WL97 were both taken from the CTIO Schmidt telescope, the improvement results because the present images represent more than 3 times longer effective exposure in  $H\alpha$ , and more than 6 times longer in the continuum, with a CCD chip that is more sensitive than the one used in 1993. Flux calibration, achieved through observations of several spectrophotometric standard stars from the list of Hamuy et al. (1992), yields a maximum surface brightness for the NW  $H\alpha$  filaments of  $2.0 \times 10^{-16} \text{ ergs cm}^{-2} \text{ s}^{-1} \text{ arcsec}^{-2}$ , a value consistent with the spectrophotometry of Ghavamian et al. (2002) when their spectrum is folded through our filter. The more diffuse emission that clearly outlines the rim of the shell to the S has surface brightness that is lower by almost a factor of 20,  $1\text{--}1.5 \times 10^{-17} \text{ ergs cm}^{-2} \text{ s}^{-1} \text{ arcsec}^{-2}$ . The large, diffuse oval that is evident within the north central portion of the shell in Fig. 5 is even fainter:  $\sim 0.6\text{--}1.4 \times 10^{-17} \text{ ergs cm}^{-2} \text{ s}^{-1} \text{ arcsec}^{-2} \approx 1\text{--}2.5 \text{ R}$  ( $1 \text{ Rayleigh} = 10^6 \text{ photons}/4\pi \text{ sr}$ ) above the nearby background sky. For comparison, the intensity of the moonless sky within our  $25 \text{ \AA}$  bandpass at the time of our observations was  $70\text{--}100 \text{ R}$ .

There is no doubt that the features shown in Figure 5 are real and not artifacts; all are evident in continuum-subtracted images from each of the two individual  $H\alpha$  filters, while deep images of other fields show no such structures. In particular, the images show that although the remnant shell is well defined at most azimuthal angles, there is diffuse emission extending inward  $\gtrsim 1/4$  of the radius. Since the lifetime of the neutral H behind the shock is quite short, it is extremely unlikely that the interior emission stems from H atoms that have penetrated that far behind the shock front; instead we must be observing material projected along the line of sight. The diffuse shell is particularly evident in the SW, where radio maps also reveal several ribbons of emission. Furthermore, the outer edge of the SNR in the NW extends well beyond the bright optical filaments, making the entire SNR more spherical

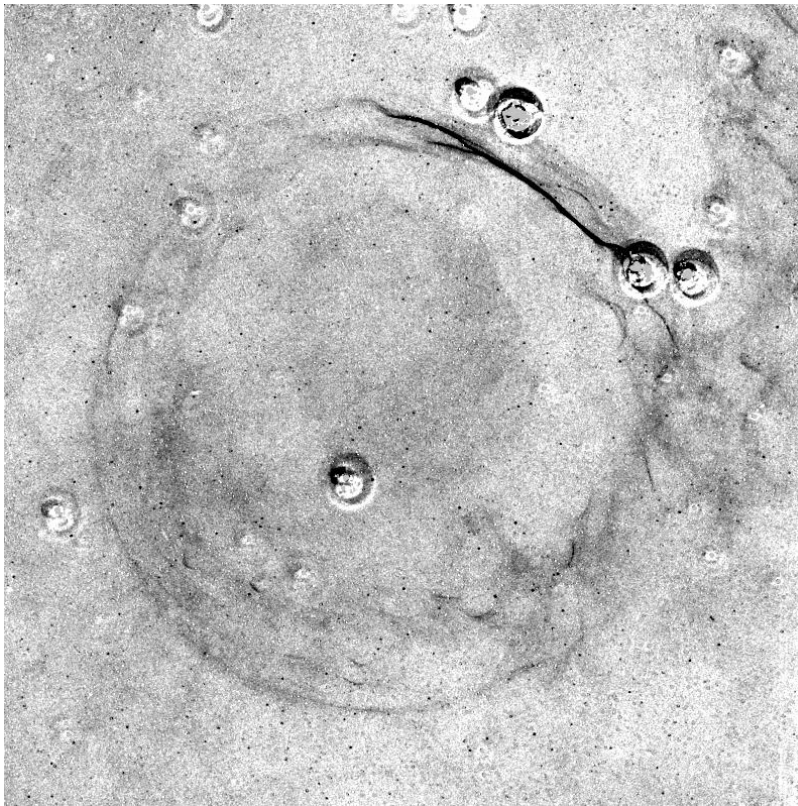


FIG. 5.— Deep  $H\alpha$  image of SN 1006 after a matched continuum image has been scaled and subtracted. In this display, the NW filaments are badly saturated in order to reveal the faint emission that outlines virtually the entire shell of the remnant. The characteristic pattern around all the bright stars is an artifact, probably resulting from microscopic imperfections in the filters. The field is exactly  $40'$  square; N is up and E to the left.

in appearance and supporting arguments that the bright filaments have arisen where the SNR shock has impacted a localized region of greater than average density.

Fig. 5 also shows diffuse emission that extends far beyond the radio or X-ray boundary of the SNR to the W and NW. Emission extends in these directions well beyond the field shown in Fig. 5 and is almost certainly diffuse foreground or background Galactic emission unrelated to SN 1006. The intensity of the diffuse emission is  $0.6\text{--}2 \times 10^{-17}$  ergs  $\text{cm}^{-2}$   $\text{s}^{-1}$   $\text{arcsec}^{-2}$ , or  $1\text{--}3$  R, which corresponds to emission measure  $\approx 2\text{--}6$   $\text{cm}^{-6}$  pc. Some of the emission within the (projected) SN 1006 shell, especially in the SW, may be an extension of this Galactic emission. Dubner et al. (2002) have conducted a search for H I 21-cm emission in the direction of SN 1006 using the Australia Telescope Compact Array. Their images, which have a resolution of about 4 arcmin, show a number of concentrations around the SNR, and it is possible that portions of these features also appear in our  $H\alpha$  images. Their total H I column map also shows an increase near the center of the SNR, which could possibly be associated with the diffuse  $H\alpha$  emission covering the central region of the shell. However, it is entirely reasonable that the central  $H\alpha$  emission is associated with SN 1006 itself, resulting from a face-on shock at the front or rear of the shell. An average of  $\sim 0.05$   $H\alpha$  photons are produced for every neutral H atom entering a shock (Chevalier & Raymond 1978), so a  $3000$   $\text{km s}^{-1}$  shock propagating along the line of sight into a region with  $n_{\text{HI}} = 0.1$   $\text{cm}^{-3}$  would produce a diffuse intensity of  $\sim 1.5$  R. In the absence of

spectroscopy, which we would expect to show Balmer lines with both narrow and very broad components for emission from the nonradiative shocks that characterize SN 1006 itself (versus only narrow lines from diffuse Galactic emission), it is impossible to resolve this issue. Spectroscopy of material within the (projected) interior that is truly associated with SN 1006 shocks would be interesting and would help to elucidate the three-dimensional geometry of the remnant, but measuring the width and center of broad Balmer lines from such faint, diffuse material will present a serious observational challenge.

We note in passing that very little if any of the emission in the image is of synchrotron origin, contrary to the suggestion by Allen et al. (2001) about our earlier (WL97)  $H\alpha$  image. Synchrotron emission should appear stronger in the matched continuum images, which have a broader bandwidth, than it does in the  $H\alpha$  ones. Instead, no diffuse emission whatsoever is evident in our continuum images, and the diffuse emission—barely visible in the  $H\alpha$  image before subtraction—becomes evident in the difference image between  $H\alpha$  and the matched continuum (Fig. 5). Furthermore, the diffuse  $H\alpha$  emission does not follow the radio or X-ray images well, contrary to what one would expect if all are of synchrotron origin.

##### 5. EXPANSION RATES AND AZIMUTHAL VARIATION

The expansion of SNRs at various stages of their development can be expressed in idealized, spherically symmetric approximations as power laws for the outer shock radius as a function of time,  $R \propto t^m$ , where  $m$  is an expansion



index. (*e.g.* Woltjer 1972; Ostriker & McKee 1988; Moffett et al. 1993; Jones et al. 1998). Very early, when the ejecta dominate over swept-up material, the ejecta expand freely and  $R \propto t$ . As the ejecta begin to encounter interstellar and circumstellar material, a reverse shock develops—stages for which Chevalier (1982) has obtained similarity solutions that give  $0.8 \gtrsim m \gtrsim 0.5$ , depending on the density dependence of the ejecta and the circumstellar material. As the reverse shock approaches the center, it disappears; the remnant becomes dominated by swept-up matter; and the expansion is described by the familiar Sedov (adiabatic) phase,  $R \propto t^{2/5}$ ,  $m = 0.4$ . Once the shock slows to a velocity  $\sim 200 \text{ km s}^{-1}$ , post-shock material can cool efficiently and a “pressure-driven snowplow” develops, for which  $m = 0.29$ . Eventually, cooling reaches the interior, the pressure drops, and the expansion approaches the simple snowplow, with  $m = 0.25$  as dictated by conservation of momentum.

For SNRs of known age  $t$ , the mean expansion index,  $m = \frac{dR}{dt} / \frac{R}{t} = \mu t / \theta$ , where  $\theta$  is the angular radius to the filament whose proper motion,  $\mu$ , has been measured, gives an indication of the evolutionary state of the remnant. Moffett et al. (1993) measured the overall expansion of the radio shell at frequencies of 1370 and 1665 GHz over a baseline of 11 years and found  $m = 0.48 \pm 0.13$ . This suggests a remnant late in its reverse-shock phase and making the transition to an ISM-dominated Sedov blast wave. Since there are no sharp radio features along the NW rim of the shell where the Balmer filaments are located, Moffett et al. were not able to measure the proper motion there and make a direct comparison with the optical value—at the time  $m = 0.33 \pm 0.04$  measured by LBV88.

Our more precise measurement of the optical proper motion leads to a refinement of the LBV88 value. For the position along the NW filaments, sectors F & G where our spectra were obtained, we measured  $\mu = 281 \pm 5 \text{ mas yr}^{-1}$ . To calculate the corresponding radius, we use the apparent center of the faint optical emission that extends almost  $180^\circ$  around the rim from NE counterclockwise to SW:  $\alpha(2000) = 15^{\text{h}}02^{\text{m}}55^{\text{s}}.4$ ,  $\delta(2000) = -41^\circ56'33''$ , a point  $\sim 40''$  east of the radio center used by Moffett et al. (1993). From our optical center, the angular radius  $\theta = 13'.6$ , and we find  $m = 0.34 \pm 0.01$ . This value suggests that in the NW portion of the shell the blast wave has encountered enough material that it is already moving beyond the Sedov phase. If the blast wave has encountered a localized, relatively dense region here, it would have slowed significantly compared with its velocity elsewhere around the shell. This in turn would produce both a lower value for  $m$  and a smaller radius to the NW filaments than the  $\theta \approx 15'$  that characterizes most of the shell—both consistent with the observations. In their H I maps, Dubner et al. (2002) have identified enhancements, just outside the SN 1006 shell to the NW, that may be interacting with the expanding shock to produce the bright filaments. The velocities of these enhancements are  $\sim -6 \text{ km s}^{-1}$  and  $\sim +10 \text{ km s}^{-1}$ , rather different from the  $\sim -25 \text{ km s}^{-1}$  predicted for material at the distance to SN 1006 based on Galactic rotation models. As Dubner et al. point out, however, one must use caution in applying circular rotation models for sources far from the Galactic plane.

It would be interesting to make a direct comparison

of optical and radio proper motions around the S and E portions of the shell. Eventually it should be possible to measure the expansion of the faint shell of Balmer emission (Fig. 5), but we will probably have to wait another decade to obtain a baseline long enough to measure the proper motion of this faint optical emission, which is far less crisp than the NW filaments that are the subject of the measurements reported in Section 3.

## 6. DISTANCE TO SN 1006

The prominent NW filaments in SN 1006 almost certainly represent sheets of material seen nearly edge-on, excited by a nonradiative shock that is moving outward almost transverse to our line of sight. From the shock velocity,  $v_s$ , and the proper motion,  $\mu$ , of the filament, the distance to SN 1006 is geometrically determined,

$$d = 2.1095 \text{ kpc} \left( \frac{v_s}{3000 \text{ km s}^{-1}} \right) \left( \frac{300 \text{ mas yr}^{-1}}{\mu} \right).$$

The width of the broad component of the Balmer lines, which results from neutral H atoms that have penetrated the shock and undergone charge exchange with hot protons, is directly proportional to the postshock proton temperature. However, the rate of electron-proton equilibration behind the shock and the pre-shock ionization structure introduce dependencies in obtaining the shock velocity. Ghavamian et al. (2002) show that the ratio of broad to narrow H $\alpha$  flux, together with the strengths of (very faint) He I and He II lines, indicates minimal equilibration at the shock front, and they obtain an unambiguous determination of the shock velocity:  $v_s = 2890 \pm 100 \text{ km s}^{-1}$ . Furthermore, the near coincidence in central wavelengths for the broad and narrow H $\alpha$  components in the Ghavamian et al. (2002) spectrum demonstrates explicitly that the shock motion is perpendicular to the line of sight, within  $\leq 2^\circ$ .

The Ghavamian et al. (2002) spectrum was taken over a portion of the filament  $51''$  long, located in sectors E and F of Fig. 2 (compare Fig. 1 of Ghavamian et al. (2002)). From Table 2, the measured proper motion of the filament in these two sectors is  $279.4 \pm 1.4$  and  $283.2 \pm 1.0 \text{ mas yr}^{-1}$ , respectively. For the proper motion of the region corresponding to the  $v_s$  measurement, we have used a simple mean,  $\mu = 281 \pm 5 \text{ mas yr}^{-1}$ , where the uncertainty is chosen conservatively to embrace some two-thirds of our measurements for *all* sectors and to allow for systematic effects. Combining the measurements leads to a geometric distance to SN 1006 of  $2.17 \pm 0.08 \text{ kpc}$ . The overall precision of 4% is limited primarily by the uncertainty in deriving the shock velocity from the measured widths of the broad Balmer lines.

Our distance estimate is consistent with, but an improvement upon, previous measurements by the same method: 1.7–3.1 kpc (LBV88); 1.4–2.8 kpc (Smith et al. 1991);  $1.8 \pm 0.3 \text{ kpc}$  (Laming et al. 1996). Ours is an improvement both because it is based on the more sensitive digital image data presented here and on the superior spectra of Ghavamian et al. (2002), and because it reflects our improved understanding of the physics of nonradiative shocks in SN 1006. In particular, LBV88 and Smith et al. (1991) allowed the possibility of full equilibration of electrons and ions behind the shock, which led to a significantly higher  $v_s$  and hence a greater distance. However,

Laming et al. (1996) and Ghavamian et al. (2002) have showed that equilibration at the shock front is minimal and hence the higher shock velocities are excluded.

Barring some fundamental misunderstanding of the physics of nonradiative shocks, our geometry-based measurement is the most reliable and precise determination of the distance to SN 1006. There are, however, other relevant data for constraining this distance. UV spectra of the Schweizer & Middleditch (1980, S-M) star, a very blue subdwarf star located near the projected center of SN 1006, show strong, very broad absorption lines of Fe II, Si II, Si IV and other ions, the result of absorption by cold, rapidly expanding SN ejecta within the SN 1006 shell (Wu et al. 1983, 1997). Obviously the S-M star must be located behind SN 1006, which sets an upper limit on the distance to the remnant. Schweizer & Middleditch (1980) classified the star as an sdOB, with color excess  $E(B - V) = 0.11$ , to obtain a distance of 0.5–2.5 kpc to the S-M star. Fesen et al. (1988) argued that the S-M star (and sdOB stars in general) is probably more luminous than Schweizer & Middleditch (1980) had estimated and obtained a distance of 1.5–3.3 kpc. More recently, Burleigh et al. (2000) classified the star as sdB, somewhat cooler but more highly absorbed with  $E(B - V) = 0.16$ , to obtain a distance estimate of 1.05–2.1 kpc. All of these estimates for the distance to the S-M star are consistent, just, with its being behind the SNR. But it is clear that a better understanding of the nature of the S-M star itself is required before estimates of its distance can be relied upon. It may be that SN 1006 and the S-M star are physically quite close together, fueling speculation that the association is more than coincidental. Savedoff & van Horn (1982) have argued convincingly that the S-M star could not have cooled fast enough to be the stellar remnant of a SN that occurred only 1000 years ago, but Burleigh et al. (2000) have speculated that it could be the stellar remnant of the donor star in an interacting binary system that produced an SN Ia event in 1006 C.E.

A second line of argument for the distance to SN 1006 also involves the S-M star, this time as the light bulb against which to observe broad UV absorption lines—and thus to obtain a “core sample” of the expanding cold material within the SN 1006 shell. Wu et al. (1993) reported Fe II velocity profiles extending to  $\pm 8300 \text{ km s}^{-1}$  at the continuum, indicating that material expanding this rapidly must still be contained within the remnant shell. Subsequently, Hamilton et al. (1997) reanalyzed the same spectra, along with new data (Wu et al. 1997), and concluded that the Fe II velocity is lower, and that the fastest material is Si II, for which they observed velocities up to  $7070 \text{ km s}^{-1}$ . Material expanding at the latter rate for 987 years (the age of the remnant at the time of the observations) will reach a radius of 7.1 pc (or 8.4 pc for the  $8300 \text{ km s}^{-1}$  velocity). If we assume spherical symmetry, SN 1006 must be at a minimum distance of 1.6 kpc (1.9 kpc) to contain this material with the  $15'$  radius of the remnant shell.

By a similar argument, the *maximum* velocity of supernova ejecta might provide an upper limit on the distance. Certainly the present radius of the SNR shell cannot exceed the distance the fastest SN ejecta would have covered had there been no deceleration. Several authors (*e.g.*

Green 1984; Fesen et al. 1988) have used a maximum velocity of  $\sim 10,000 \text{ km s}^{-1}$  to obtain an upper limit on the distance,  $d \lesssim 2.3 \text{ kpc}$ . Recent observations (*e.g.* Hatano et al. 1999) and theory (*e.g.* Hoefflich et al. 1998) show that velocities of  $16,000$ – $20,000 \text{ km s}^{-1}$ , and sometimes higher, are found in SN Ia ejecta. The requirement that the average expansion velocity of the shell be  $\lesssim 20,000 \text{ km s}^{-1}$  requires only that  $d \lesssim 4.6 \text{ kpc}$ —no longer a meaningful constraint.

The distance to SN 1006 has been recently discussed by several authors (Strom 1988; Willingale et al. 1996; Schaefer 1996; Laming et al. 1996, WL97). In addition to the kinematic arguments discussed above, other distance estimates to SN 1006 have relied heavily on models for the X-ray emission and parameters such as the post-shock temperature and interstellar density that are highly uncertain and variable around the remnant shell. The rich X-ray structure seen in recent *Chandra* images (Long et al. 2002) make it obvious that earlier models, most of which rely on simple spectra and spherical symmetry, are vastly oversimplified. We conclude that the measurement of  $2.17 \pm 0.08 \text{ kpc}$  presented here is not only consistent with all present data, but is also both more precise and more accurate than previous distance estimates.

## 7. HOW BRIGHT WAS SN 1006?

The supernova that was first witnessed on or about 1006 May 1 is generally acknowledged to have become (within a few days) the brightest supernova recorded in human history. Despite its southerly declination,  $\delta(1006) \approx -38^\circ 5'$ , clear records of its sudden appearance are found in contemporary chronicles from Egypt, Iraq, Italy, Switzerland, China, and Japan, with additional references that may refer to sightings of the star from France, Syria, and elsewhere. Interesting excursions through the historical records and their interpretation may be found in Shklovskii (1968), Stephenson et al. (1977), Clark & Stephenson (1977), Devorkin (1985), and references in these sources. Recorded observations are much more numerous and widespread than for the far more favorably positioned (for northern observers) SN 1054 that occurred only 48 years later and that produced the Crab Nebula. The peak magnitude for SN 1006 has been variously estimated at values ranging from  $\sim -5$  to  $-10$ , based on different interpretations of the historical accounts (see below).

Once upon a time, astronomers sought to shed light on the Hubble constant by combining the brightness at maximum of SN 1006 and of other historical supernovae with the modern distances to their remnants to estimate peak absolute magnitudes. These estimates then served as a method for obtaining the distances to extragalactic SNe. Although recorded sightings of SN 1006 by eleventh-century observers are numerous, photometric “calibration” of their observations has proved fraught with ambiguity for modern readers, as the wide variation in interpretation of the same records attests. Fortunately, the Cepheid distance scale has now been extended to include the host galaxies of several well-observed supernovae with good photometry. We can thus run the old argument in reverse, using current values for SN peak absolute magnitudes and the distance to SN 1006 to estimate just how

bright it was at maximum. Laming et al. (1996) have followed an argument similar to the one below, but with different, more uncertain, values both for the distance to SN 1006 and for its absolute magnitude at maximum.

While we cannot be certain of the type for SN 1006, it is generally assumed to have been Type Ia. Arguments include its location, at Galactic latitude  $14^\circ 6'$ ,  $\sim 550$  pc above the plane, the presence of at least a few tenths  $M_\odot$  of Fe within its shell (Hamilton et al. 1997), the absence of any evidence for a compact stellar remnant, the lack of any massive star association anywhere in the vicinity, and the implication from at least one Chinese historical record, the *Sung Shih*, official history of the Sung dynasty (960–1279), that it remained visible for several years (Goldstein & Ho 1965). Saha et al. (2001) give peak absolute magnitudes for 9 SNe Ia in galaxies with well-determined Cepheid distances, and find the mean V-band absolute magnitude at maximum light (uncorrected for decline rate) to be  $M_V^{max} = -19.55$ , with an RMS dispersion of 0.09. Both Branch (1998) and Gibson et al. (2000) have used almost the same data set with somewhat different calibration procedures to arrive at mean absolute magnitudes of  $-19.44$  and  $-19.47$ , respectively, and a dispersion of 0.12 in the latter case. A fairer representation of the actual dispersion in peak luminosities of SNe Ia is probably that based on a sample of 29 uniformly observed SNe Ia in the the Calan-Tololo survey (Hamuy et al. 1996), for which  $\Delta M_V^{max} = 0.26$ . Correction based on the rate of decline (Phillips 1993) would reduce the dispersion, but the decline rate is of course not known for SN 1006. We will adopt here a peak luminosity for SN Ia events corresponding to  $M_V^{max} = -19.50 \pm 0.40$ , where the uncertainty should be generous enough to include both uncertainties in the calibration and the intrinsic dispersion among the events themselves.

The reddening to the S-M star was estimated by Schweizer & Middleditch (1980) as  $E(B - V) = 0.112 \pm 0.024$ , and the visual extinction as  $A_V = 0.32 \pm 0.10$ . Wu et al. (1993) used the UV spectrum of the S-M star to obtain essentially the same value:  $E(B - V) = 0.10 \pm 0.02$ , corresponding to  $A_V = 0.31 \pm 0.06$ . Since the star must be beyond, but probably not far beyond, SN 1006, we adopt the same extinction value for the remnant with somewhat higher uncertainty:  $A_V = 0.31 \pm 0.10$ .

Assuming that SN 1006 was, in fact, a Type Ia event and using the above values for peak SN Ia luminosity, and the distance and extinction to SN 1006, we conclude, *a posteriori*, that at its brightest, SN 1006 reached peak visual magnitude  $-7.5 \pm 0.4$ . The uncertainty is a purely formal one, and is dominated by that in the peak SN Ia luminosity.

Our value falls squarely in the middle of the widely varying estimates based on historical records. Most of these have relied heavily on the same text by the Egyptian astrologer Ali bin Ridwan (d. 1061), in a commentary on Ptolemy's *Tetrabiblos* rediscovered by Goldstein (1965), of the remarkable stellar spectacle that Ali bin Ridwan recalled from his youth. As translated from the Arabic by Goldstein, this reads in part,

I will now describe for you a spectacle that  
I saw at the beginning of my education.  
... (*he describes the location, in opposition*

*to the Sun*) ... It was a large spectacle, round in shape, and its size  $2\frac{1}{2}$  or 3 times the magnitude of Venus. Its light illuminated the horizon and it twinkled very much. The magnitude of its brightness was a little more than a quarter of the brightness of the Moon. ...

This passage has been variously interpreted to arrive at quantitative estimates for the magnitude of SN 1006 at maximum. Goldstein (1965) focused on comparison with the Moon and reasoned that the peak brightness was comparable to that of the Moon quarter-illuminated ( $-8$ ) or half-illuminated (quarter phase,  $-10$ ). Stephenson et al. (1977) argue that the comparison should be made with the full Moon. Changing light levels have a subjective effect approximating the square root of the intensity, so the maximum brightness of the star would have been about  $1/15$  that of the full Moon, or magnitude  $-9.5$ . (Stephenson et al. also invoke other arguments based on this and other texts to support the same estimate.) Pskovskii (1978) argued that the star must have been  $2\frac{1}{2}$  or 3 magnitudes brighter than Venus and used the modern magnitude scale to arrive at  $-6 \pm 0.5$ . Independent of the Ali bin Ridwan text, Schaefer (1996) has estimated the peak magnitude based on historical records of the heliacal setting and rising of SN 1006 in August and November of 1006, respectively. By comparison with a variety of template light curves for SNe Ia, he estimates a peak magnitude between  $-4.1$  and  $-6.7$ .

There is another, very straightforward interpretation of the Ali bin Ridwan text that gives a result remarkably similar to our current estimate. Suppose that we assume that “its size  $2\frac{1}{2}$  or 3 times the magnitude of Venus,” and “the magnitude of its brightness was a little more than a quarter of the brightness of the Moon,” both refer to the *same* sort of relative measurement, on a logarithmic scale analogous to the modern (and also the ancient, approximately) magnitude scale. That is, Venus and the Moon represent points of comparison, and the spectacle in question is  $2\frac{1}{2}$  or 3 steps brighter than Venus, and 4 steps fainter than the Moon. On the evening of 1006 May 1, the new star appeared in opposition to the Sun, while the Moon was only one day past new and thus was not visible. At the full Moon two weeks later, however, the supernova was probably near its peak brightness. Toward the end of twilight, the full Moon, SN 1006, and Venus would all have been visible  $\sim 15^\circ$  above the horizon in different directions. It seems entirely plausible that this memorable array would have prompted Ali bin Ridwan to make the comparison quoted above—using Venus and the Moon as benchmarks to gauge the brightness of the star. At the time, Venus would have had  $V \approx -4.0$ , and the full Moon  $V \approx -12.5$  (Stephenson et al. 1977). If we divide the magnitude range  $V = -4.0$  to  $-12.5$  into 6.5 (7) equal steps, and take the SN 1006 magnitude as 2.5 (3) steps brighter than Venus, we find a result  $V_{SN} \approx -7.3$  ( $-7.6$ ). This interpretation seems at least as plausible as any other, and agrees remarkably well with our estimate based on modern data.

While a peak brightness of  $-7.5$  is significantly fainter than the more extravagant of past estimates based on historical data, certainly an event of magnitude  $-7.5$  would

have been bright enough to attract wide attention, as indeed SN 1006 did throughout the world in the eleventh century.

P.F.W. and K.S.L. gratefully acknowledge the outstanding support, typical of the mountain staff at CTIO, during the observations that yielded the new data reported here. We thank F. D’Arcangelo for her assistance in reduction of the Schmidt data, J. D. Emerson for sharing his insight into some statistical questions, and M. Kamal for

translation and elucidation of the Arabic texts relating to SN 1006. This work has been made possible through the financial support from the NSF, through grant AST-961845 to P.F.W., and from NASA, through grants NAG 5-8020 to P.F.W. and *Chandra* grants GO0-1120X and GO1-2058A to K.S.L. Additional support for astrophysics research at Middlebury College has been provided by the W.M. Keck Foundation through the Keck Northeast Astronomy Consortium.

## REFERENCES

- Allen, G. E., Petre, R., & Gotthelf, E. V. 2001, *ApJ*, 558, 739  
 Avni, Y. 1976, *ApJ*, 210, 642  
 Bevington, P. R. & Robinson, D. K. 1992, *Data Reduction and Error Analysis for the Physical Sciences*, 2nd edition (New York: McGraw-Hill), 71  
 Branch, D. 1998, *ARA&A*, 36, 17  
 Burleigh, M. R., Heber, U., O’Donoghue, D., & Barstow, M. A. 2000, *A&A*, 356, 585  
 Chevalier, R. A. 1982, *ApJ*, 258, 790  
 Chevalier, R. A., Kirshner, R. P., & Raymond, J. C. 1980, *ApJ*, 235, 186  
 Chevalier, R. A. & Raymond, J. C. 1978, *ApJ*, 225, L27  
 Clark, D. H. & Stephenson, F. R. 1977, *The Historical Supernovae* (Oxford: Pergamon), 114–139  
 Devorkin, D. H. 1985, *Astronomy Quarterly*, 5, 71  
 Dubner, G. M., Giacani, E. B., Goss, W. M., Green, A. J., & Nyman, L.-Å. 2002, *A&A*, 387, 1047  
 Fesen, R. A., Wu, C., Leventhal, M., & Hamilton, A. J. S. 1988, *ApJ*, 327, 164  
 Fruchter, A. S. & Hook, R. N. 2002, *PASP*, 114, 144  
 Gardner, F. F. & Milne, D. K. 1965, *AJ*, 70, 754  
 Ghavamian, P., Winkler, P. F., Raymond, J. C., & Long, K. S. 2002, *ApJ*, 572, 888  
 Gibson, B. K., et al. 2000, *ApJ*, 529, 723  
 Goldstein, B. R. 1965, *AJ*, 70, 105  
 Goldstein, B. R. & Ho, P. Y. 1965, *AJ*, 70, 748  
 Green, D. A. 1984, *MNRAS*, 209, 449  
 Hamilton, A. J. S., Fesen, R. A., Wu, C.-C., Crenshaw, D. M., & Sarazin, C. L. 1997, *ApJ*, 481, 838  
 Hamuy, M., Phillips, M. M., Suntzeff, N. B., Schommer, R. A., Maza, J., & Aviles, R. 1996, *AJ*, 112, 2391  
 Hamuy, M., Walker, A. R., Suntzeff, N. B., Gigoux, P., Heathcote, S. R., & Phillips, M. M. 1992, *PASP*, 104, 533  
 Hatano, K., Branch, D., Fisher, A., Baron, E., & Filippenko, A. V. 1999, *ApJ*, 525, 881  
 Hesser, J. E. & van den Bergh, S. 1981, *ApJ*, 251, 549  
 Hoeflich, P., Wheeler, J. C., & Thielemann, F. K. 1998, *ApJ*, 495, 617  
 Jones, T. W., et al. 1998, *PASP*, 110, 125  
 Koyama, K., Petre, R., Gotthelf, E. V., Hwang, U., Matsuura, M., Ozaki, M., & Holt, S. S. 1995, *Nature*, 378, 255  
 Laming, J. M., Raymond, J. C., McLaughlin, B. M., & Blair, W. P. 1996, *ApJ*, 472, 267  
 Lampton, M., Margon, B., & Bowyer, S. 1976, *ApJ*, 208, 177  
 Long, K., Dyer, K., Petre, R., Raymond, J., Reynolds, S., Wang, U., & Winkler, F. 2002, in preparation  
 Long, K. S., Blair, W. P., & van den Bergh, S. 1988, *ApJ*, 333, 749  
 McKee, C. F. & Hollenbach, D. J. 1980, *ARA&A*, 18, 219  
 Moffett, D. A., Goss, W. M., & Reynolds, S. P. 1993, *AJ*, 106, 1566  
 Ostriker, J. P. & McKee, C. 1988, *Reviews of Modern Physics*, 60, 1  
 Phillips, M. M. 1993, *ApJ*, 413, L105  
 Pskovskii, I. P. 1978, *AZh*, 55, 737  
 Reynolds, S. P. & Gilmore, D. M. 1986, *AJ*, 92, 1138  
 Saha, A., Sandage, A., Tammann, G. A., Dolphin, A. E., Christensen, J., Panagia, N., & Macchetto, F. D. 2001, *ApJ*, 562, 314  
 Savedoff, M. P. & van Horn, H. M. 1982, *A&A*, 107, L3  
 Schaefer, B. E. 1996, *ApJ*, 459, 438  
 Schweizer, F. & Lasker, B. M. 1978, *ApJ*, 226, 167  
 Schweizer, F. & Middleditch, J. 1980, *ApJ*, 241, 1039  
 Shklovskii, I. S. 1968, *Supernovae* (London: Wiley-Interscience), 45–49  
 Smith, R. C., Kirshner, R. P., Blair, W. P., & Winkler, P. F. 1991, *ApJ*, 375, 652  
 Stephenson, F. R., Clark, D. H., & Crawford, D. F. 1977, *MNRAS*, 180, 567  
 Strom, R. G. 1988, *MNRAS*, 230, 331  
 Tanimori, T., et al. 1998, *ApJ*, 497, L25  
 Tonry, J. & Davis, M. 1979, *AJ*, 84, 1511  
 van den Bergh, S. 1976, *ApJ*, 208, L17  
 Willingale, R., West, R. G., Pye, J. P., & Stewart, G. C. 1996, *MNRAS*, 278, 749  
 Winkler, P. F. & Laird, F. N. 1976, *ApJ*, 204, L111  
 Winkler, P. F. & Long, K. S. 1997, *ApJ*, 491, 829  
 Woltjer, L. 1972, *ARA&A*, 10, 129  
 Wu, C., Crenshaw, D. M., Fesen, R. A., Hamilton, A. J. S., & Sarazin, C. L. 1993, *ApJ*, 416, 247  
 Wu, C., Crenshaw, D. M., Hamilton, A. J. S., Fesen, R. A., Leventhal, M., & Sarazin, C. L. 1997, *ApJ*, 477, L53  
 Wu, C.-C., Leventhal, M., Sarazin, C. L., & Gull, T. R. 1983, *ApJ*, 269, L5  
 Zacharias, N., et al. 2000, *AJ*, 120, 2131